Supplementary Information for

" Super-resolution femtosecond electron diffraction reveals electronic and nuclear dynamics at conical intersections "

Hui Jiang[1,2,3†], Juanjuan Zhang[4†], Tianyu Wang[2,3†], Jiawei Peng[4], Cheng Jin[2,3], Xiao zou[2,3], Pengfei Zhu[1,2], Tao Jiang[2,3], Zhenggang Lan[4*], Haiwang Yong[5*], Feng He[2*], Dao Xiang[1,2,3*]

[1]Tsung-Dao Lee Institute, Shanghai Jiao Tong University, Shanghai 201210, China.

[2]Key Laboratory for Laser Plasmas (Ministry of Education) and School of Physics and Astronomy, Collaborative innovation center for IFSA (CICIFSA), Shanghai Jiao Tong University, Shanghai 200240, China.

[3]Zhangjiang Institute for Advanced Study, Shanghai Jiao Tong University, Shanghai 201210, China.

[4]SCNU Environmental Research Institute, Guangdong Provincial Key Laboratory of Chemical Pollution and Environmental Safety, MOE Key Laboratory of Environmental Theoretical Chemistry, School of Environment, South China Normal University, Guangzhou 510006, China.

[5]Department of Chemistry and Biochemistry, University of California San Diego, La Jolla, CA 92093, USA.

[*]Corresponding authors: zhenggang.lan@m.scnu.edu.cn (Zhenggang Lan); hyong@ucsd.edu (Haiwang Yong); fhe@sjtu.edu.cn (Feng He); dxiang@sjtu.edu.cn (Dao Xiang)

[†]These authors contributed equally to this work.

This file includes:

Supplementary Note 1: Diffraction pattern processing

Our data processing follows the below workflow.

1. Detector mask. A mask is generated for each image. All pixels outside the phosphor screen region are masked out and the hot pixels are removed.

2. Background subtraction. A diffraction pattern is collected with the same integration time before delivering the sample to the gas cell.This image is then used as the background. Each loaded pattern is then subtracted from this background.

3. Determination of the diffraction center. The center of each image is determined by fitting a ring to the pixels within a certain intensity range (typically 1500-2000 counts).

4. Alignment of the patterns. All patterns are aligned based on the centers obtained from the fitting.

5. Normalization. All patterns are normalized based on the total counts within a certain momentum transfer range (1-10 Å^{-1}).

6. Average. Images at the same delay are averaged. Then, the averaged patterns for all time delays are obtained, forming a set of data.

7. Bootstrap. A total of 300 patterns are randomly selected and averaged for each time delay to generate a new dataset. This sampling process is repeated 200 times, and the resulting 200 datasets are used to estimate the experimental uncertainty.

8. Radial integration. The salt and pepper noise is removed by performing 2D median filtering. Then, the one-dimensional scattering intensity $I(s,t)$ is obtained by radial averaging around the diffraction center.

The above procedures delineate the method for obtaining the 1D $I(s,t)$ from the 2D measured diffraction pattern. The static scattering intensity $I(s,t<0)$ comprises the molecular scattering signal $I_m(s,t<0)$, atomic scattering signal $I_a(s,t<0)$ and other background $I_b(s,t<0)$. To extract $I_m(s,t<0)$, we follow the methods used by Ihee[1]. First, zero points of $I_m^{\text{sim}}(s,t<0)$ from theoretical results are calculated. Then, we fit the values of $I(s,t<0)$ at these zero points with a low-order polynomial. The fitted curve contains both the background and atomic scattering signals. Finally, the static molecular scattering intensity $I_m(s,t<0)$ is obtained by subtracting the fitted curve from $I(s,t<0)$. The modified scattering intensity (sM) is computed by the following

equation:

$$\mathrm{sM}(s) = \frac{I_m(s, t < 0)}{I_a} s, \tag{1}$$

The atomic scattering intensity is calculated as follows:

$$I_a = \sum_i^N f_i^*(s) f_i(s) \tag{2}$$

where $f_i(s)$ is the elastic scattering amplitude for the ith atom and is calculated by the ELSEPA program[2].

The difference scattering intensity is computed as follows:

$$\Delta I(s, t) = I(s, t) - I(s, t < 0). \tag{3}$$

Both the background and the atomic signal are subtracted without further processing. Then the modified difference scattering intensity can be calculated as follows:

$$\Delta\mathrm{sM}(s, t) = \frac{\Delta I(s, t)}{I_a} s. \tag{4}$$

Due to the relatively low signal-to-noise ratio in the high-s region, a baseline modification to $\Delta\mathrm{sM}(s > 5.5$ Å) by fitting a low-order polynomial to the signal is used, similar to the method used by other groups[1,3]. The $\Delta\mathrm{sM}(s, t)$ before and after the correction are shown in Supplementary Fig. 8.

Supplementary Note 2: Linear absorption range

In order to minimize the impact of multiphoton absorption and ionization on the experimental results, it is necessary to carefully select the pulse energy for the UV pump laser. To this end, the integrated absolute intensity of $I(t = 2$ ps$) - I(t = -1$ ps$)$ at $1.5 < s < 6$ Å^{-1} was measured under varying laser intensities. The results are shown in Supplementary Fig. 9. The intensity exhibited a linear relationship with the pulse energy. In this study, the pulse energy was maintained at approximately 50 μJ, which is within the linear region.

Supplementary Note 3: Details in pair distribution function (PDF) transform

In the measured static $\mathrm{sM}(s)$, the signals at $s < 0.8$ Å^{-1} are not measured due to the central hole of the phosphor screen. Additionally, the procedure of removing the background by polynomial fit-

ting mentioned above cannot accurately eliminate the background signal at small scattering angles, leading to deviations between the experimental and theoretical values at $0.8 < s < 1.3$ Å^{-1}. This Unremoved background signal may be attributed to the unscattered electron beam. Noted that the background signals can be naturally eliminated when calculating the difference signals. To circumvent the occurrence of non-physical outcomes stemming from the truncation of the low-s region when computing the static PDF, scaled simulation results are used to supplement the data within the range of $0 < s < 1.3$ Å^{-1}.

For the modified difference scattering intensity $\Delta\mathrm{sM}(s,t)$, although the background has been subtracted when computing ΔI, the inelastic scattering signals in the low-s region ($s < 1.3$ Å^{-1}) can still affect the structural information. Thus, we fill $\Delta\mathrm{sM}(s,t)$ in the range of 0-1.3 Å^{-1} by extrapolation of the experimental data. We fit the $\Delta\mathrm{sM}(s)$ at $1.3 < s < 4$ Å^{-1} with the model:

$$\mathrm{sM}_{\mathrm{extra}}(s) = \sum_{k=1}^{N} \alpha_k \frac{\sin(sr_k)}{sr_k} s, \tag{5}$$

in which α_k and r_k are the optimization parameters. In consideration of the asymptotic behavior of $\Delta\mathrm{sM}(s)$ at $s = 0$, we impose the constraint $\sum_{k=1}^{N} \alpha_k = 0$ and N is set to 4. Subsequently, the $\Delta\mathrm{sM}(s)$ signals at $0 < s < 1.3$ Å^{-1} are filled by the fitting function. The complete $\Delta\mathrm{sM}(s,t)$ after extrapolation is shown in Supplementary Fig. 10 where the inelastic scattering signals have been removed. We compare the $\Delta\mathrm{PDF}(r, t = 1\ \mathrm{ps})$ calculated by two different integration intervals ($1.3 < s < 10$ Å^{-1} and $0 < s < 10$ Å^{-1}), as shown in Supplementary Fig. 11. It can be seen that filling the signals at $s < 1.3$ Å^{-1} only results in a slight change in the intensity of certain peaks without affecting the overall characteristics of ΔPDF.

It is important to note that all the methods described above for filling sM at low-s region are not required in the super-resolved inversion technique.

Supplementary Note 4: Super-resolved pair distribution function (s-PDF) transform

Here, we provide a concise overview of the procedures employed to achieve super-resolution [4] in this experiment.

1. Discretization in momentum and real space. A schemed discretization is applied in the real-

space inversion:

$$\begin{cases} s_i = \frac{j_{0i}}{j_{0N}} N\Delta s, & 1 < i < N \\ R_m = \frac{j_{0m}}{M\Delta s}, & 1 < m < M \end{cases} \tag{6}$$

in which j_{0i} is the ith root of j_0 (the zeroth-order spherical Bessel function of the first kind). In this study, the discrete spacing in momentum space, denoted by Δs, is set to 0.1 Å^{-1}. Given the maximum effective s-range ($\sim$ 10 Å^{-1}), N is set to 101 and therefore $s_{max} = N\Delta s = 10.1$ Å^{-1}. M=ceil($\pi/(\Delta R \Delta s)$)+1. ΔR is chosen to be 0.05 Å, and the corresponding super-resolution factor is $M/N \approx 6$.

2. Window function. The window function $h(s)$ is chosen to be the same as that for computing PDF:

$$h(s) = \begin{cases} e^{-ks^2}, & s_{min} < s < s_{max} \\ 0, & s < s_{min} \end{cases} \tag{7}$$

Given the effective s-range, k is set to 0.03 Å^2. In the super-resolution inversion approach, we take $s_{min} = 1.3$ Å^{-1} and therefore we no longer need to fill the scattering signals in the low-s region ($s < 1.3$ Å^{-1}), as was done in the PDF transform.

3. Dictionary of natural scattering kernel (NSK). Super-resolution reconstructs the original pair distance density ($\rho(R)$) with a series of weighted δ-function pair distance density. NSK corresponds to the real-space transformation of individual δ-function density ($\rho(R) = \delta(R - R_{m^*})$)

$$\text{NSK}_{m^*}(R_m) = \frac{[(M-1)\Delta s]^2}{j_{0M}} \sum_{i=1}^{M-1} G_{mi} j_0(s_i R_{m^*}) s_i h(s_i), \tag{8}$$

$$G_{mi} = 2\frac{j_0(\frac{j_{0m}j_{0i}}{j_{0M}})}{j_{0M} j_1^2(j_{0i})}. \tag{9}$$

Then the dictionary is composed of a set of NSKs along the real-space sampling R_{m^*}:

$$\mathcal{D} = \begin{bmatrix} \text{NSK}_{1^*}(R_1) & \cdots & \text{NSK}_{m^*}(R_1) & \cdots & \text{NSK}_{M^*}(R_1) \\ \vdots & & \vdots & & \vdots \\ \text{NSK}_{1^*}(R_m) & \cdots & \text{NSK}_{m^*}(R_m) & \cdots & \text{NSK}_{M^*}(R_m) \\ \vdots & & \vdots & & \vdots \\ \text{NSK}_{1^*}(R_M) & \cdots & \text{NSK}_{m^*}(R_M) & \cdots & \text{NSK}_{M^*}(R_M) \end{bmatrix}. \tag{10}$$

4. Inversion of scattering signals. The discretized scattering signals are converted to the pair distribution function in real space by:

$$\Delta\mathrm{PDF}(R_m, t) = \frac{[(M-1)\Delta s]^2}{j_{0M}} \sum_{i=1}^{M-1} G_{mi} \frac{\Delta I(s_i, t)}{f_e(s_i)} s_i h(s_i), \tag{11}$$

where $\Delta I(s,t)$ is the diffraction signals that contains the structural information. In the case of static structures, $\Delta I(s,t)$ corresponds to the molecular diffraction signal. Similarly, for time-resolved structural changes, it refers to the difference diffraction signals. $f_e(s)$ is the effective atomic scattering factor and is estimated by $f_e(s) = f_a^*(s) f_b(s)$, where a and b refer to the main types of atoms. In this study, C-C pair distances dominate, and as a result, $f_e(s)$ is set to $f_C^*(s) f_C(s)$.

5. Deconvolution of ΔPDF. The dictionary generated above is used to deconvolute ΔPDF by minimizing:

$$||\Delta\mathrm{PDF} - \mathcal{D}\boldsymbol{w}||^2 + \alpha\mathcal{R}(\boldsymbol{w}), \tag{12}$$

where $\mathcal{R}(\boldsymbol{w}) = \sum_m |\boldsymbol{w}_m|$. This l_1 regularizer[5] gives us sparse weighted δ-function pair density with $\boldsymbol{w}_m$ being the weight. α is determined by the corner of L-curve[6]. The convex optimization is performed with a package[7]. For static s-PDF, we impose the constraint $\boldsymbol{w}_m \geq 0$.

To understand the meaning of the intensity of s-PDF, we consider a simple case when the molecule only consists of one type of atom. In this case, Eq. (11) can be further simplified to:

$$\Delta\mathrm{PDF}(R_m, t) = \frac{[(M-1)\Delta s]^2}{j_{0M}} \sum_{i=1}^{M-1} \sum_R G_{mi} \Delta\rho(R, t) j_0(s_i R) s_i h(s_i), \tag{13}$$

where $\Delta\rho(R,t)$ refers to the difference pair charge density. Comparing Eq. (13) with the NSK (8), we can see that $\boldsymbol{w}(m) \approx \Delta\rho(R = R_m, t)$ if R is sparse. Therefore, the super-resolved intensity directly reflects the pair density for molecules comprising solely one type of atom. For molecules comprising different types of atoms, the super-resolved intensity is proportional to the pair density and the product of scattering cross sections of the atom pairs.

The validity of the deconvolution can be further substantiated by employing the L-curve method depicted in Supplementary Fig. 12. The L-shaped curves in both the static s-PDF and Δs-PDF justify the choice of l_1 regularizer.

Supplementary Note 5: Static C-H pair distribution

The static scattering signals encode the ground-state CHD structural information with a high signal-to-noise ratio. The super-resolution technique facilitates the reconstruction of diverse interatomic distances, including all C-C and C-H interatomic distances for static structures. As previously mentioned, the super-resolved peak intensities are proportional to the product of the pair density and the scattering cross sections of the atom pairs. To facilitate comparison with s-PDF, here the distribution of the interatomic distance in the static structures obtained through theoretical sampling is scaled with the scattering cross sections of the atomic pairs and shown in Supplementary Fig. 13. To gain more insights, we separate the different types of atomic pairs. As shown in Supplementary Fig. 13b, the C-C interatomic distances exhibit three distinct peaks corresponding to R_1, R_2 and R_3. The C-H interatomic distances in Supplementary Fig. 13c exhibit peaks at 1.05, 2.1, 3.5, and 3.9 Å, corresponding to the 1st, 2nd, 3rd, and 4th C-H interatomic distances, respectively. The small peak near 2.9 Å overlaps with the R_3 C-C pair distance. The weight of the H-H interatomic distances in Supplementary Fig. 13d is too small to be clearly observed. Nevertheless, the reconstruction of characteristic C-H pair distances has been accomplished with high fidelity, underscoring the distinct advantage of s-PDF in achieving high spatial resolution.

Supplementary Note 6: Background subtraction of the inelastic scattering signal

The intensity of the inelastic scattering signal is obtained by integrating over the $0.8 < s < 1.05$ Å^{-1} region in ΔsM, as shown in Supplementary Fig. 14a. While the signal's primary origin is inelastic scattering, it also contains contributions from elastic scattering and the residual background. Consequently, we subtract the extrapolated elastic scattering signals and the remaining constant background signals which may be induced by the ionization effects, and the modified inelastic scattering signals are shown in Supplementary Fig. 14b. It is evident that these procedures exert minimal influence on the rising edge of the signal, with only a small effect on the fitted decay time constant at the falling edge.

Supplementary Note 7: The influence of different atomic pairs on the interpretation of CI dynamics.

Since the scattering signals are dominated by carbon atoms, we focus on the influence of C-C pairs on structural dynamics. In addition to the analyzed C_1-C_6 pair, Supplementary Figure 15 shows the evolution of C_1-C_2 (nearest) and C_1-C_3 (next-nearest) obtained using the simulated trajectories. The dynamics of these two interatomic distances can help us assess the impact of molecular distortions beyond the contributions from the C_1-C_6 pair and explain why the evolution of C_1-C_6 was used to qualitatively analyze the characteristic changes in atomic pair density near 1.95 Å and 2.3 Å within the first 100 fs, respectively.

We first consider the Δs-PDF near 1.95 Å. As shown in Supplementary Fig. 15a, in the absence of C_1-C_6 pair, the nearest atomic pairs arising from molecular distortion or vibration typically contribute to signals below 1.75 Å, and thus have minimal impact at 1.95 Å. Also, Supplementary Figure 15b shows that next-nearest pairs generally influence regions beyond 2.1 Å, indicating that their contribution to the 1.95 Å signal is also negligible. Therefore, the feature at 1.95 Å primarily originates from the early-stage opening of the C_1-C_6 pair, as it approaches and crosses the 1.95 Å region.

Since the excess kinetic energy of the molecule reaches its maximum after the electronic state decays to its ground state, structural distortions and vibrational motions are not pronounced during the early stage of the CI passage. As shown in Supplementary Fig. 15b, d, the evolution of the next-nearest pair remains largely unchanged within the first 80 fs. Significant C_1-C_3 oscillations only appear after the wave packet passes through the second CI, when the molecule gains substantial kinetic energy. Therefore, although the Δs-PDF feature near 2.3 Å lies within the typical range of R_2, during the initial 80 fs of CI dynamics, the signal arising from molecular distortions is relatively weak. The observed knee feature at ~2.3 Å in the Δs-PDF is primarily attributed to the progressive elongation of the C_1-C_6 pair distance approaching this distance.

For these reasons, we use the evolution of the C_1-C_6 pair to qualitatively illustrate the structural dynamics near the conical intersections.

Supplementary Note 8: Effect of temporal resolution on imaging the CI dynamics

In order to facilitate a reliable comparison between experiment and theory, all the simulated results in this study have been convoluted with the instrument response function (IRF) of the measurement. The s-PDF analysis reveals that the time for the wave packet to traverse through the two CIs is approximately 30 fs, which is smaller than the IRF (about 80 fs). While resolving a time-delay smaller than the IRF of the measurement is not uncommon, this analysis is only feasible when the temporal resolution is sufficiently high. To illustrate the effect of temporal resolution on the extracted information of the CI dynamics, the simulated intensity of the Δs-PDF at ~1.95 Å and ~2.30 Å with various IRF is shown in Supplementary Fig. 16. The results indicate that when the IRF is larger than 120 fs, the characteristic features employed for CI dynamics extraction vanish. In this study, the 80-fs IRF provides the sufficient resolution to resolve both the characteristic structures of Δs-PDF at ~1.95 Å and ~2.30 Å, which are crucial for extracting the traversal time between the two CIs.

Supplementary Note 9: Effect of *s*-range on imaging the CI dynamics

To simultaneously minimize the influence of inelastic scattering and enhance spatial resolution, we chose a relatively small lower limit $s = 1.3$ Å^{-1}. To validate whether different choices of the *s*-range affect the observed CI structural dynamics, here we show the structural dynamics during passage through the two CIs calculated by two different *s*-ranges in Supplementary Fig. 17. The lower limit of the momentum transfer used for the Δs-PDF transformation is set to 1.5 Å^{-1} in Supplementary Fig. 17a, c and 1.7 Å^{-1} in Supplementary Fig. 17b, d. By comparing with the results in Fig. 4a, c of the main text, we find that varying the lower limit of the *s*-range has no noticeable effect on the characteristic features observed in the Δs-PDF evolution (knee structure). These findings indicate that our results are robust against different *s*-ranges. Qualitatively, this robustness arises because the dynamics near the conical intersection involve relatively small structural changes, which primarily contribute to scattering signals at larger scattering angles.

Supplementary References

[1] Ihee, H., Goodson, B. M., Srinivasan, R., Lobastov, V. A. & Zewail, A. H. Ultrafast electron diffraction and structural dynamics: transient intermediates in the elimination reaction of c_2 f_4 i_2. *The Journal of Physical Chemistry A* **106**, 4087–4103 (2002).

[2] Salvat, F., Jablonski, A. & Powell, C. J. Elsepa—dirac partial-wave calculation of elastic scattering of electrons and positrons by atoms, positive ions and molecules. *Computer Physics Communications* **165**, 157–190 (2005).

[3] Yang, J. *et al.* Simultaneous observation of nuclear and electronic dynamics by ultrafast electron diffraction. *Science* **368**, 885–889 (2020).

[4] Natan, A. Real-space inversion and super-resolution of ultrafast scattering. *Phys. Rev. A* **107**, 023105 (2023).

[5] Tibshirani, R. Regression shrinkage and selection via the lasso. *Journal of the Royal Statistical Society Series B: Statistical Methodology* **58**, 267–288 (1996).

[6] Hansen, P. C. & O'Leary, D. P. The use of the l-curve in the regularization of discrete ill-posed problems. *SIAM Journal on Scientific Computing* **14**, 1487–1503 (1993).

[7] Udell, M. *et al.* Convex optimization in Julia. *SC14 Workshop on High Performance Technical Computing in Dynamic Languages* (2014). `1410.4821`.

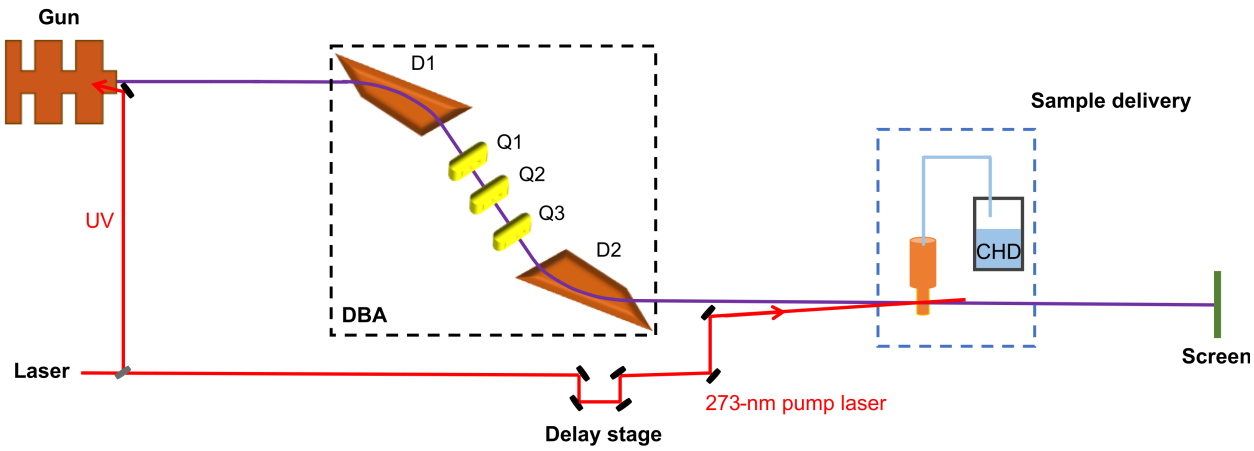

Supplementary Fig. 1: **Experimental setup.** The focused 273-nm laser pulse intersects with the electron beam on the sample delivered via a flow cell. The electron beam is compressed by a double bend achromat (DBA) which consists of two dipole magnets (D1 and D2) and three quadrupole magnets (Q1, Q2 and Q3) to reduce both the bunch length and arrival time jitter. The instrument response function in this experiment was ~80 fs (FWHM).

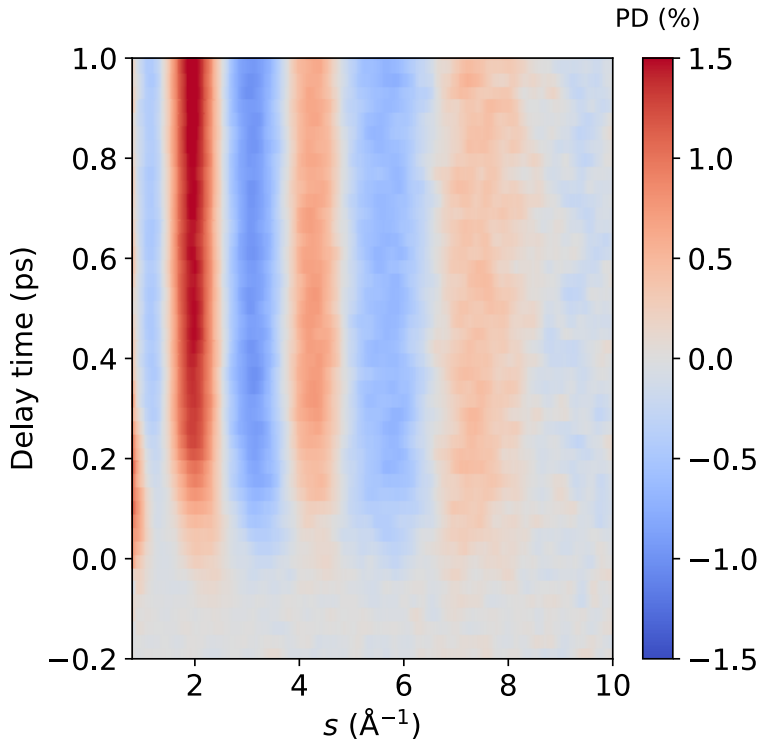

Supplementary Fig. 2: **The full data set of experimental percentage difference signal.**Source data are provided as a Source Data file.

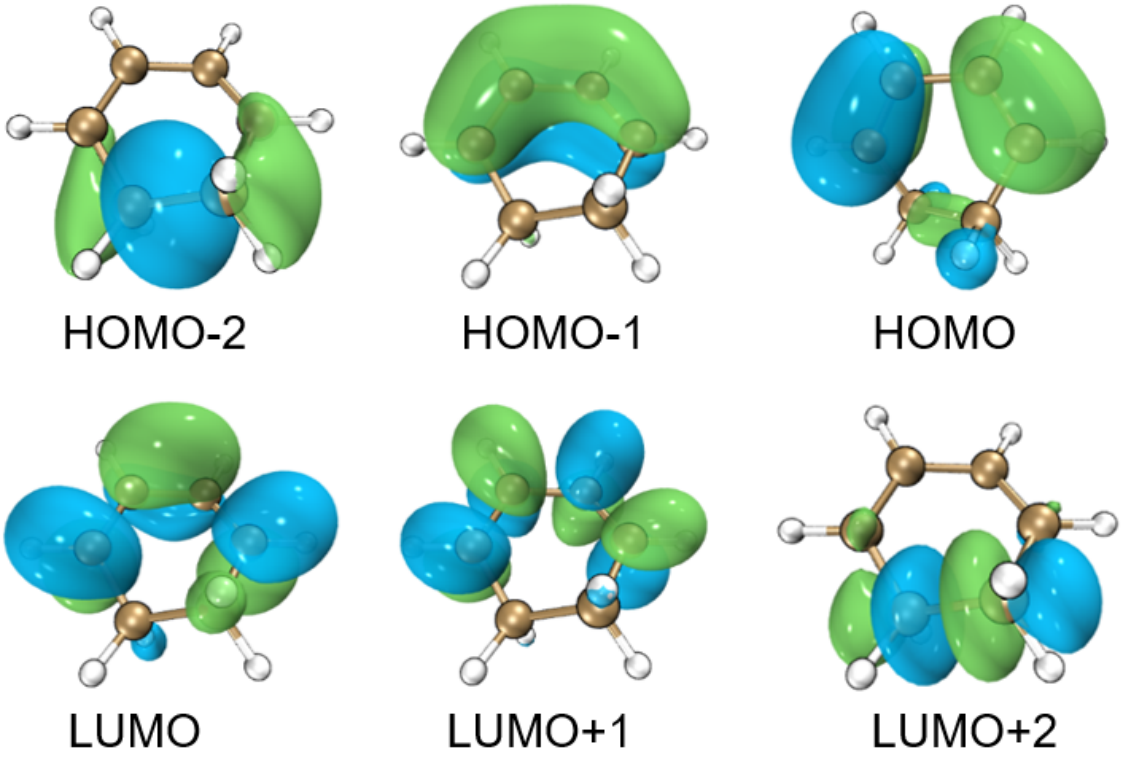

Supplementary Fig. 3: **Active space orbitals in the XMS (3)-CASPT2(6, 6)/def2-TZVP calculations.**

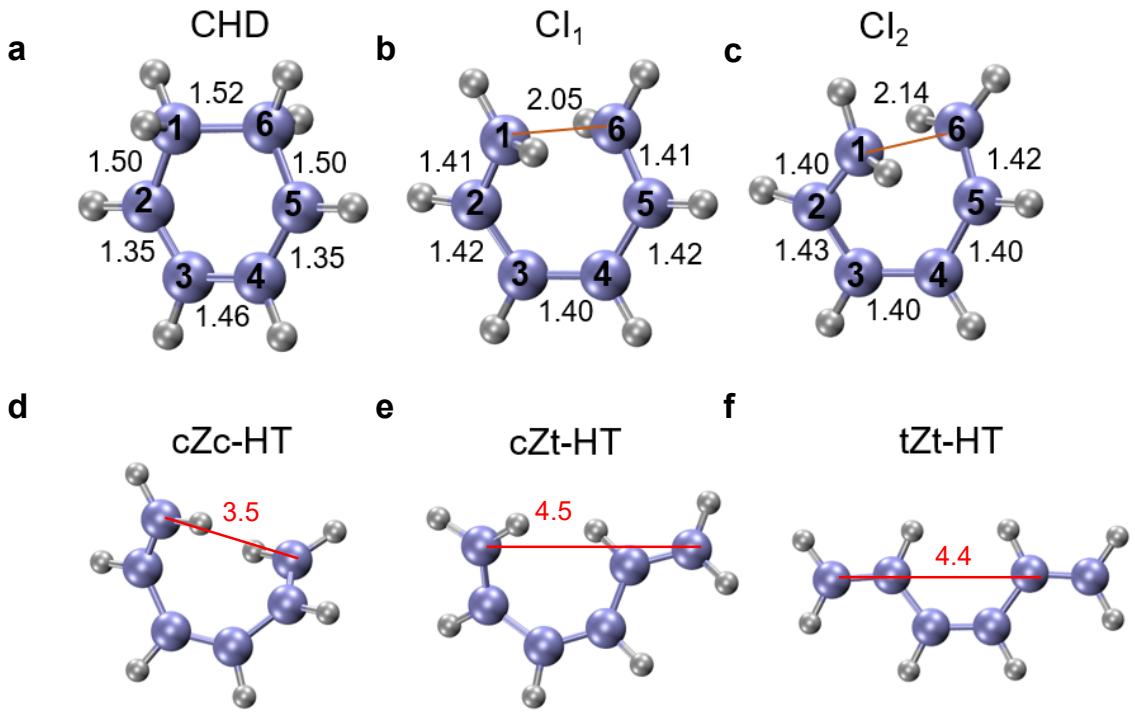

Supplementary Fig. 4: **The optimized geometries of S_0-min, CI_1, CI_2 and three HT isomers.** **a**, S_0-min. **b**, CI_1. **c**, CI_2. **d**, cZc-HT. **e**, cZt-HT. **f**, tZt-HT. Interatomic distances are given in units of Å. Source data are provided as a Source Data file.

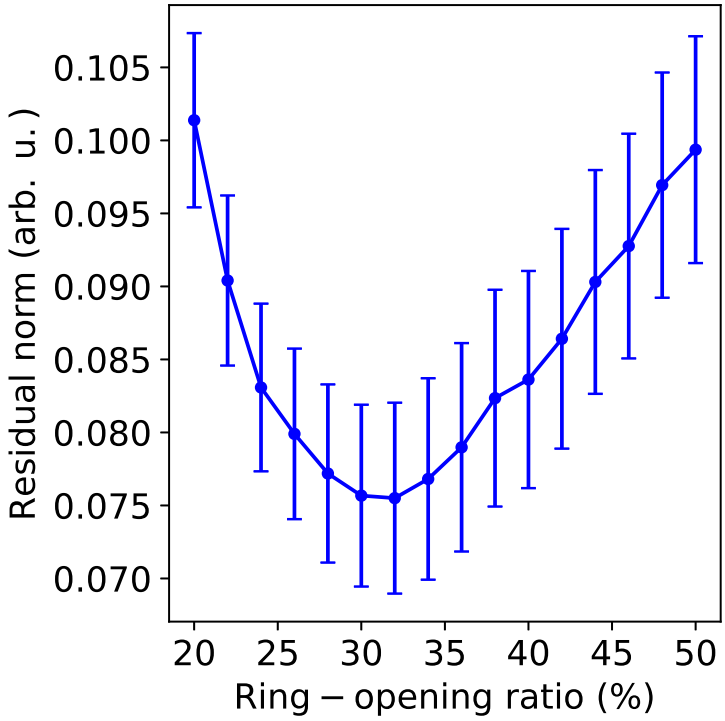

Supplementary Fig. 5: **Estimation of the quantum yield of HT.** The residual norm under different ring-opening ratios is defined as the difference between the simulated and measured values of the ΔsM over the same time interval, with the simulated values calculated using different ring-opening ratios. Error bars represent a 68% confidence interval. Source data are provided as a Source Data file.

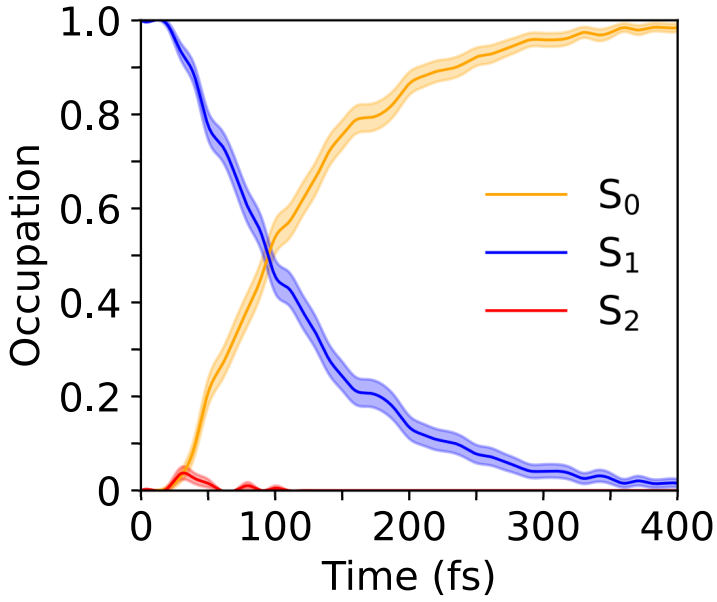

Supplementary Fig. 6: **The population evolutions of excited states as a function of delay time in the nonadiabatic simulation.** The uncertainties of these curves are given by the Bootstrap method.

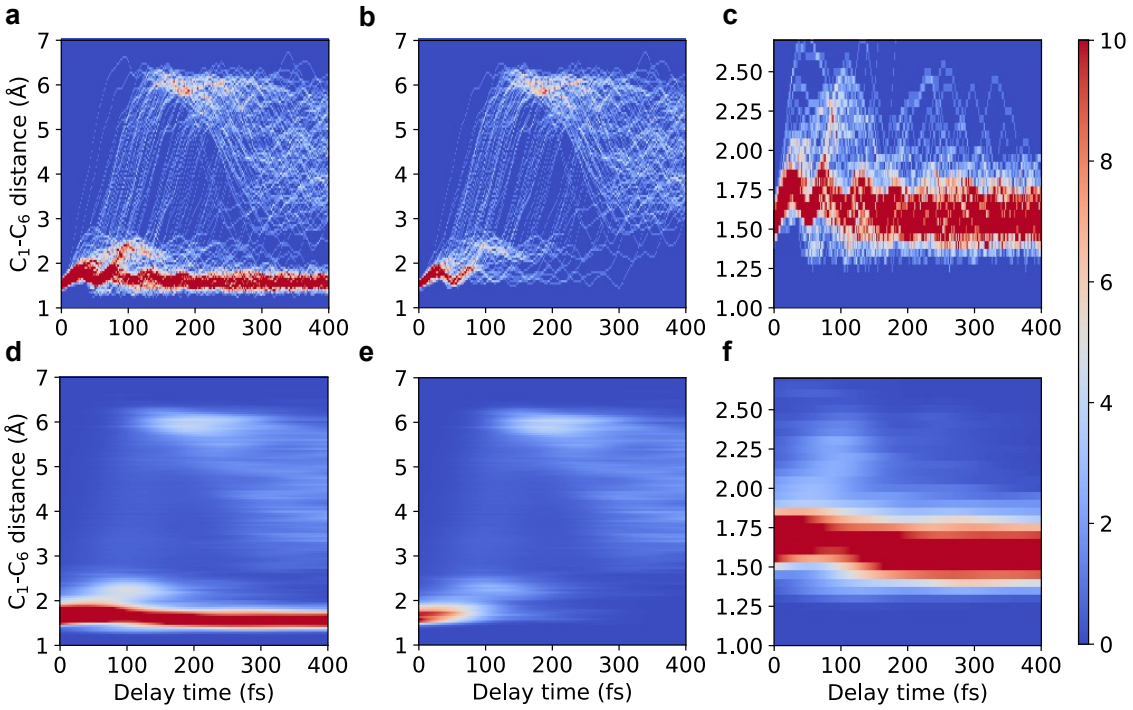

Supplementary Fig. 7: **Simulated evolutions of the C_1–C_6 interatomic distance. a**, All 193 trajectories. **b**, Ring-opening trajectories. **c**, Ring-closing trajectories. **d**-**f**, The same sets of trajectories shown in panels **a**-**c**, respectively, after convolution with a Gaussian function (80-fs FWHM) to account for temporal resolution. Source data are provided as a Source Data file.

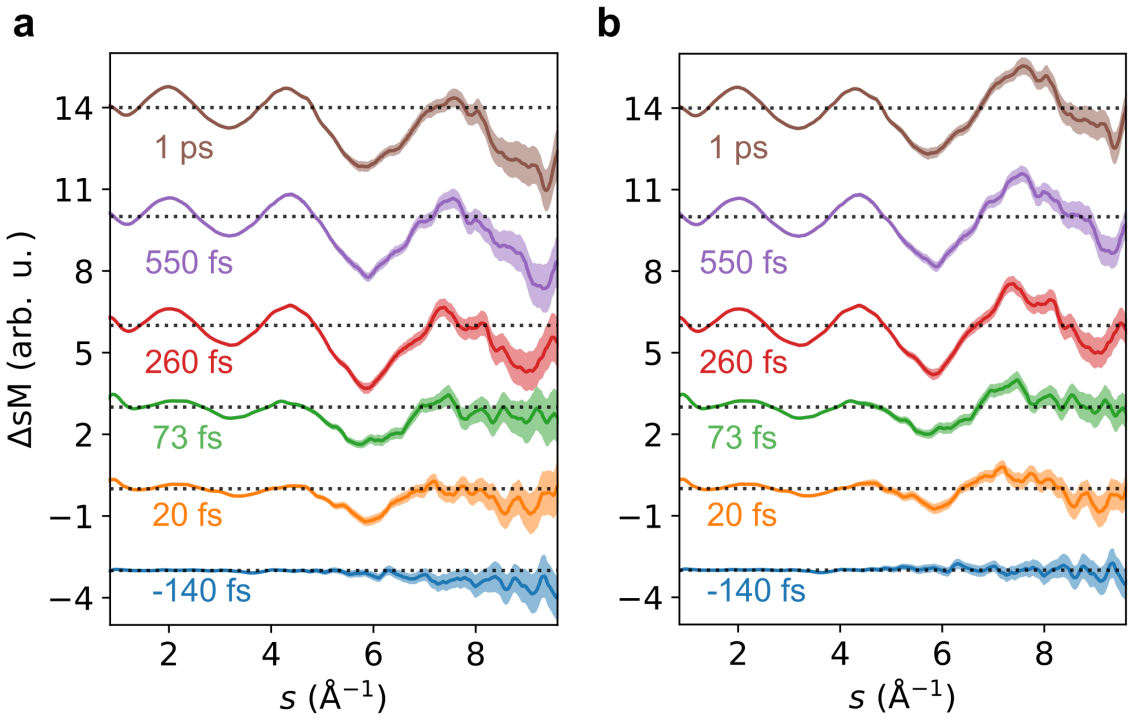

Supplementary Fig. 8: **Baseline modification for high-s signals. a** and **b**, The ΔsMs at six selected time points before and after the baseline modification by a low-order polynomial fit performed on ΔsM in the range of $s > 5.5$ Å^{-1}, respectively. The black dotted lines are the baselines for each curve. The uncertainties are calculated by the bootstrap method and the shaded regions denote the 68% confidence interval. Source data are provided as a Source Data file.

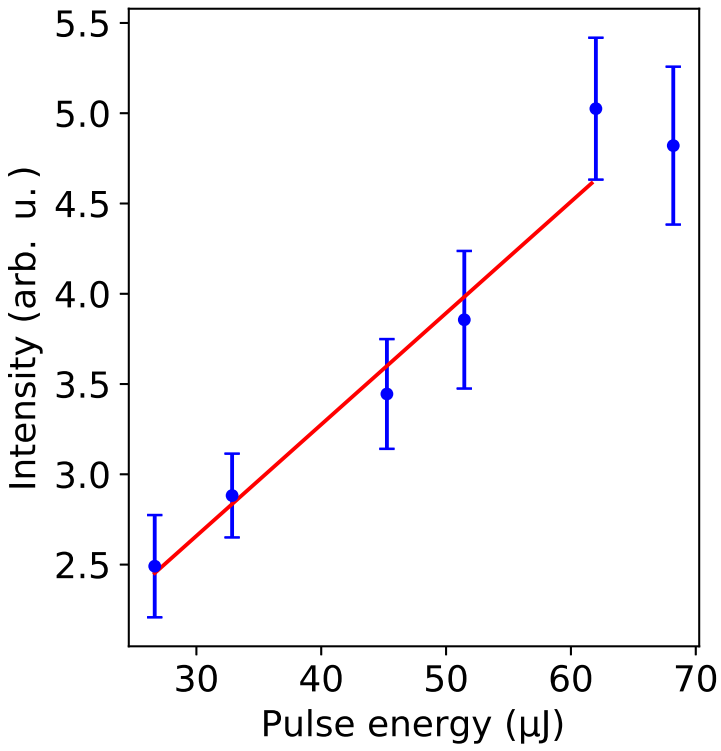

Supplementary Fig. 9: **The pump pulse energy scan.** Correlation between the integrated absolute diffraction intensity change in the range of $1.5 < s < 6$ Å^{-1} and the UV pulse energy. Error bars represent a 68% confidence interval. Source data are provided as a Source Data file.

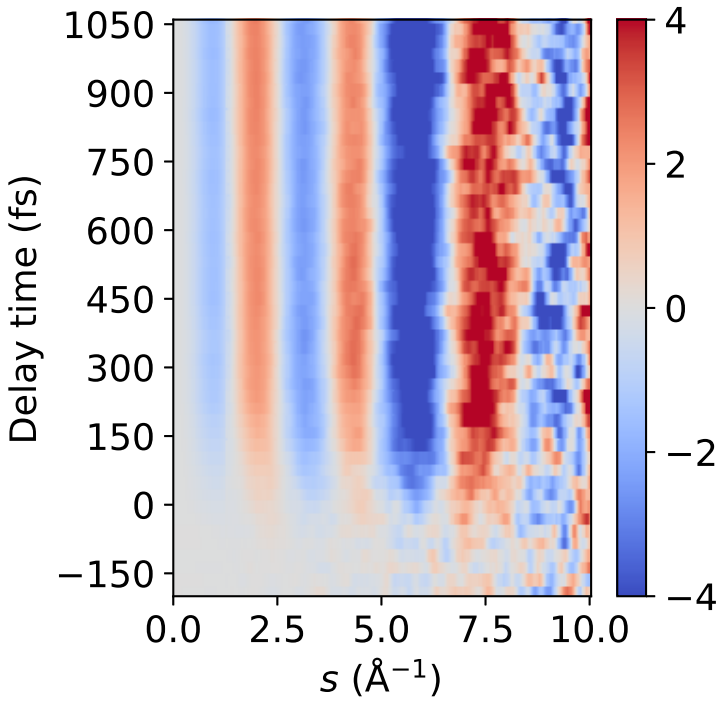

Supplementary Fig. 10: **Extrapolation of elastic scattering signals.** The measured elastic scattering ΔsM involves the removal of the original signals at $s < 1.3$ Å^{-1}, which contain inelastic scattering, and the supplementation of these signals with extrapolations derived from experimental data within the range of $1.3 < s < 4$ Å^{-1}. Source data are provided as a Source Data file.

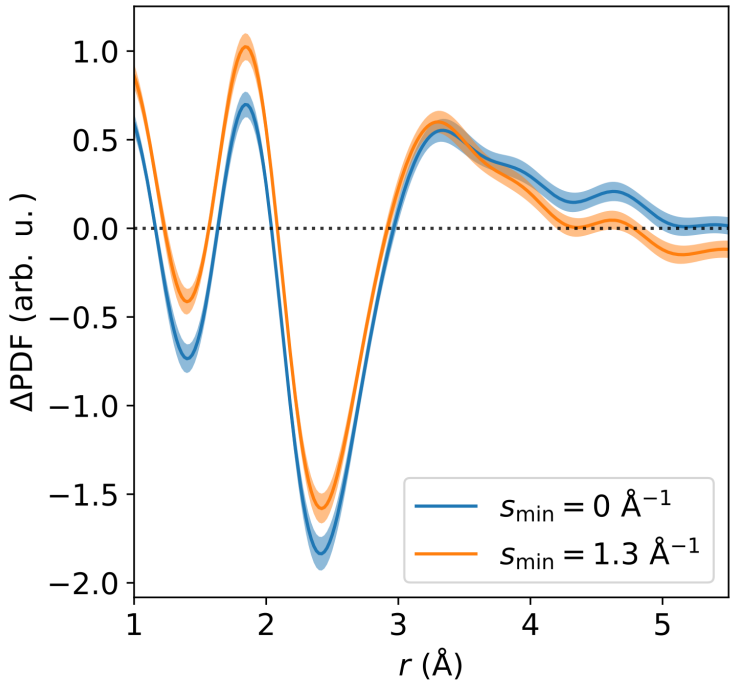

Supplementary Fig. 11: **ΔPDFs computed with different *s*-range.** The orange and blue lines represent the ΔPDFs before and after the extrapolation of low-*s* elastic scattering signals, respectively. The shaded regions denote the 68% confidence interval. Source data are provided as a Source Data file.

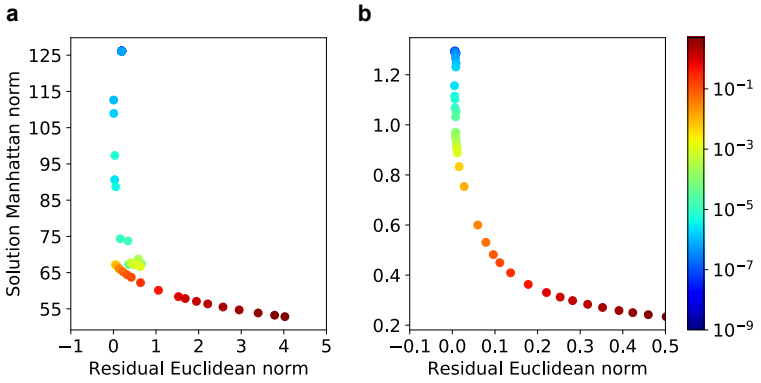

Supplementary Fig. 12: **The L-curve representations in optimizations of static s-PDF and Δs-PDF.** The L-curves, which plot the trade-off between the residual norm and solution Manhattan norm when computing static s-PDF in **a** and Δs-PDF in **b**, are used to determine the regularization parameters and verify the choice of the regularization. The regularization parameter α is set near the corner of the L-shaped curve. Source data are provided as a Source Data file.

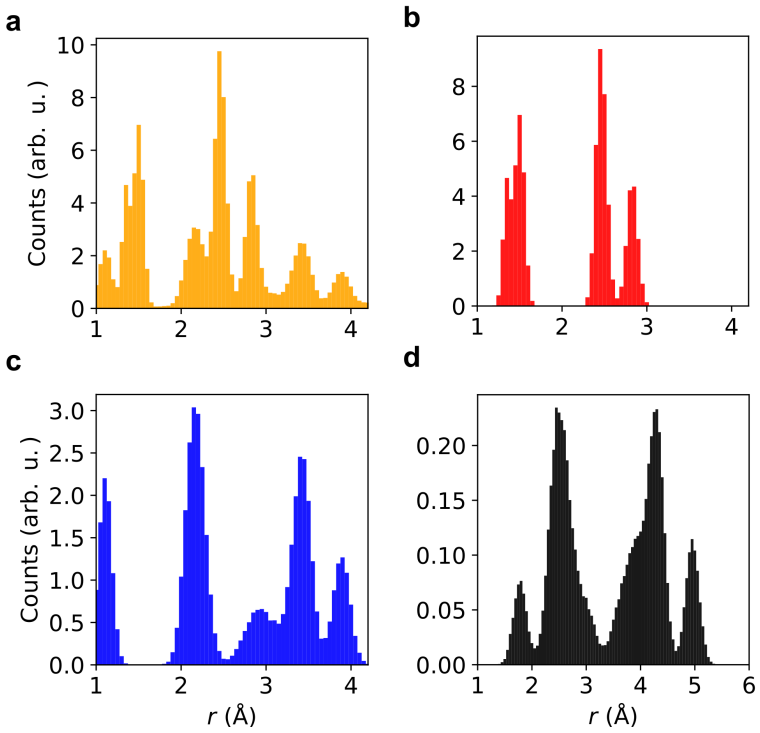

Supplementary Fig. 13: **The pair distance distribution of static simulated structures. a**, All pair distances. **b**, C-C pair distances. **c**, C-H pair distances. **d**, H-H pair distances. A total of 5,000 conditions sampled from the Wigner distribution function of the lowest vibrational state at the S_0-min are counted. The count of each pair distance is scaled by the product of their atomic scattering amplitudes. Source data are provided as a Source Data file.

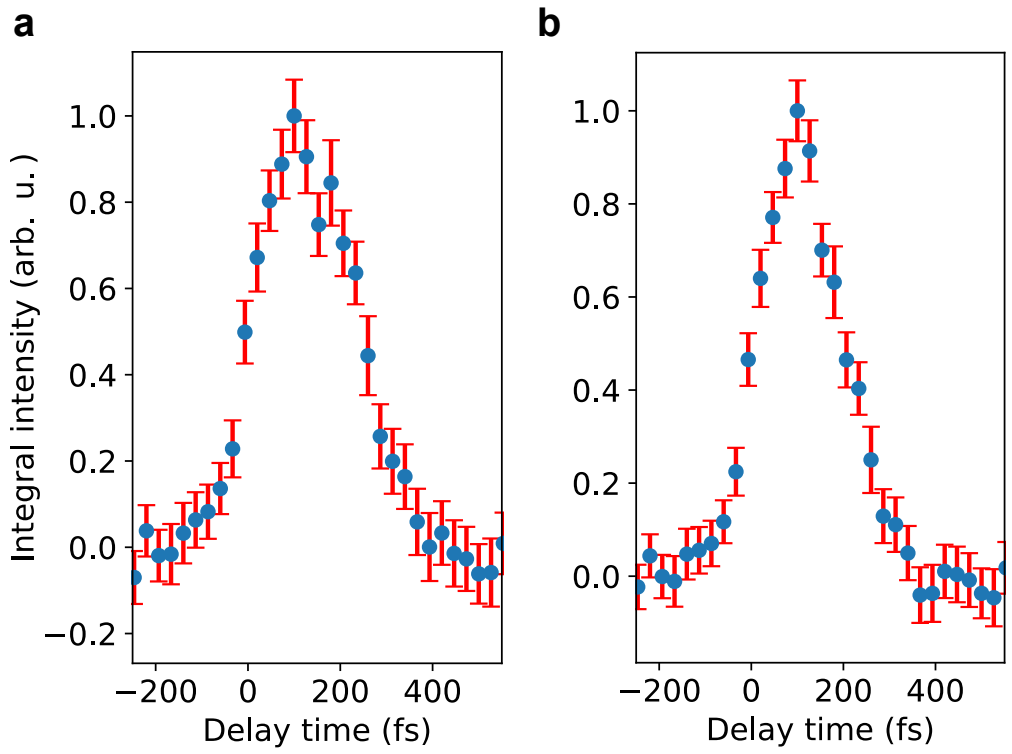

Supplementary Fig. 14: **Background removal of the inelastic scattering signal. a**, The original integrated intensity of small-angle signals at $0.8 < s < 1.05$ Å^{-1}. **b**, The modified integrated intensity after removing the elastic signals and the additional background. Error bars represent a 68% confidence interval. Source data are provided as a Source Data file.

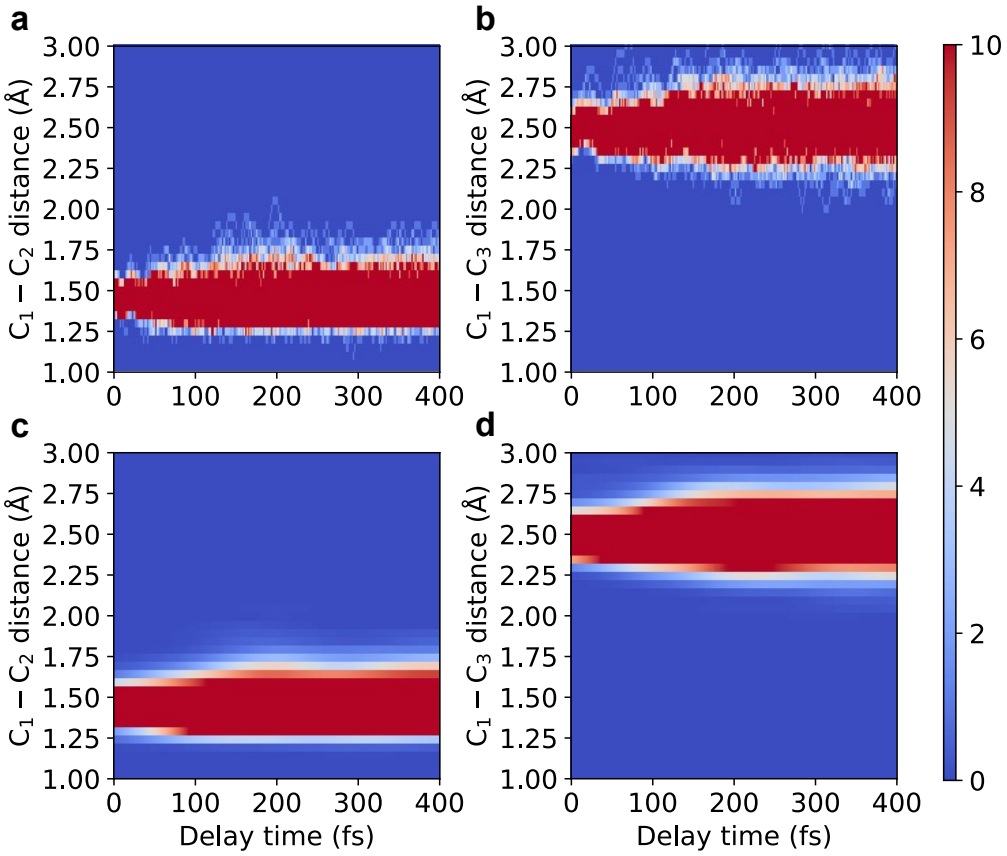

Supplementary Fig. 15: **Simulated evolutions of C_1–C_2 and C_1–C_3 interatomic distances from all 193 trajectories.** Atomic labels are shown in Fig. 1b. C_1–C_2 refers to a nearest carbon pair, while C_1–C_3 corresponds to a next-nearest pair. **a** and **c**, The evolution of C_1–C_2 before and after temporal convolution. **b** and **d**, The evolution of C_1–C_3 before and after temporal convolution. Source data are provided as a Source Data file.

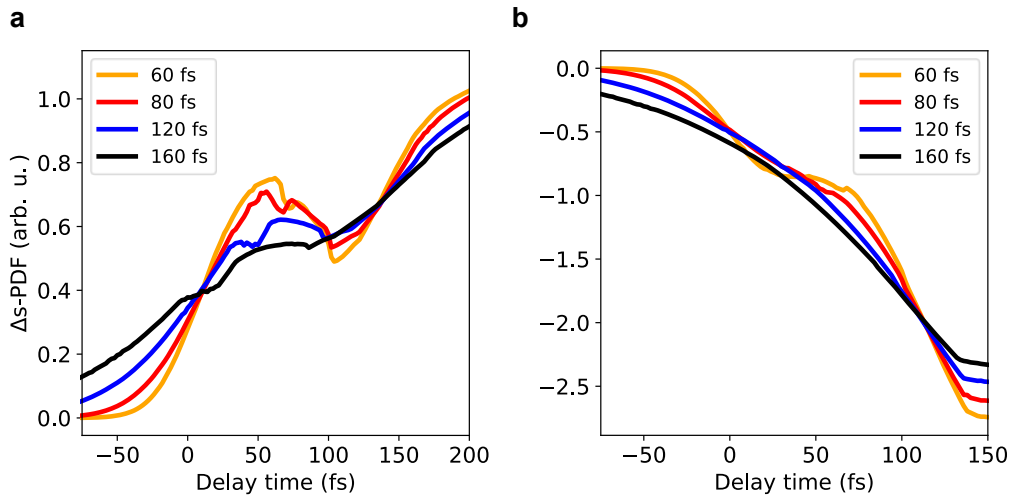

Supplementary Fig. 16: **Simulated Δs-PDF after convolution with Gaussian kernels of various width. a** and **b**, Simulated intensity of Δs-PDF at ~1.95 Å and ~2.30 Å, respectively. The simulated results are convoluted with Gaussian kernels of 60 fs (orange), 80 fs (red), 120 fs (blue) and 160 fs (black) to illustrate the effect of temporal resolution in extracting the information of the CI dynamics. Source data are provided as a Source Data file.

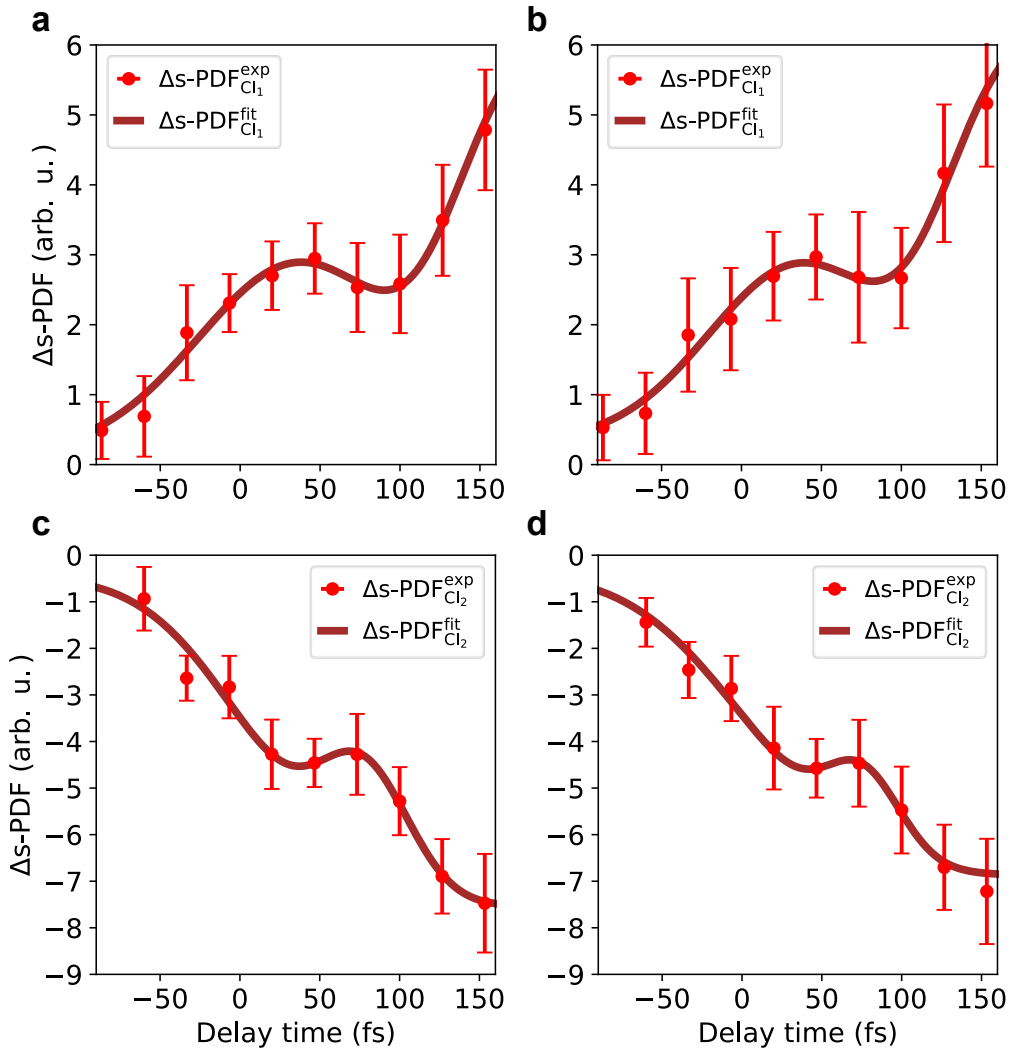

Supplementary Fig. 17: **Structural dynamics during passage through the two CIs calculated by two different *s*-ranges. a** and **c**, Measured intensity of Δs-PDF at ~1.95 Å and ~2.30 Å, respectively. The lower limit is taken as 1.5 Å^{-1}. b and d, Measured intensity of Δs-PDF at ~1.95 Å and ~2.30 Å, respectively. The lower limit is taken as 1.7 Å^{-1}. Error bars represent a 68% confidence interval calculated from bootstrap sampling. Source data are provided as a Source Data file.

Supplementary Table 1: **The energies of three lowest electronic states at S_0-min, CI_1, and CI_2.** The energy of the ground state minimum of CHD is set to zero.

Geometries	S_0 (eV)	S_1 (eV)	S_2 (eV)
S_0-min	0	4.95	6.29
CI_1	2.74	4.23	4.23
CI_2	3.66	3.66	5.89

Supplementary Table 2: **Characters of two low-lying electronic states.** The vertical excitation energies (VEEs), oscillator strength (f) and electronic characters of two low-lying electronic states at the XMS (3)-CASPT2 (6, 6)/def2-TZVP level at S_0-min of CHD.

	VEEs (eV)	f	Dominant Contributions
S_1	4.95	0.16378	HOMO→LUMO (Single excitation)
S_2	6.29	0.00197	HOMO→LUMO (Double excitation)
			HOMO-1→LUMO (Single excitation)